Journal of Solid State Chemistry 183 (2010) 814–822

Contents lists available at ScienceDirect

Journal of Solid State Chemistry

journal homepage: www.elsevier.com/locate/jssc

Syntheses, optical properties and electronic structures of copper(I) tantalates: $Cu_5Ta_{11}O_{30}$ and $Cu_3Ta_7O_{19}$

Olena Palasyuk, Andriy Palasyuk, Paul A. Maggard *

Department of Chemistry, 2620 Yarbrough Drive, North Carolina State University, Raleigh, NC 27695-8204, USA

ARTICLE INFO

Article history:
Received 10 November 2009
Received in revised form
25 January 2010
Accepted 30 January 2010
Available online 4 February 2010

Keywords:
Copper tantalates
Solid-state synthesis
Flux synthesis
Optical properties

ABSTRACT

Two copper tantalates, $Cu_5Ta_{11}O_{30}$ (**1**) and $Cu_3Ta_7O_{19}$ (**2**), were synthesized by solid-state and flux synthetic methods, respectively. A synthetic route yielding **2** in high purity was found using a CuCl flux at 800°C and its structure was characterized using powder X-ray diffraction (XRD) data ($P6_3/m$ (no. 176), $Z=2$, $a=6.2278(1)$ Å, and $c=20.1467(3)$ Å). The solid-state synthesis of **1** was performed using excess Cu_2O that helped to facilitate the growth of single crystals and their characterization by XRD ($P\bar{6}2c$ (no. 190), $Z=2$, $a=6.2252(1)$ Å, and $c=32.516(1)$ Å). The atomic structures of both copper tantalates consist of alternating single and double layers of TaO_7 pentagonal bipyramids that are bridged by a single layer of isolated TaO_6 octahedra and linearly-coordinated Cu^+. Measured optical bandgap sizes of ~2.59 and ~2.47 eV for **1** and **2** were located well within visible-light energies and were consistent with their orange–yellow colours. Each also exhibits optical absorption coefficients at the band edge of ~700 and ~275 cm^{-1}, respectively, and which were significantly smaller than that for $NaTaO_3$ of ~1450 cm^{-1}. Results of LMTO calculations indicate that their visible-light absorption is attributable mainly to indirect bandgap transitions between Cu $3d^{10}$ and Ta $5d^0$ orbitals within the TaO_7 pentagonal bipyramids.

1. Introduction

Metal oxides have attracted an intense amount of research interest owing to their photocatalytic production of H_2 and/or O_2 from water, which is driven by their bandgap excitations, as highlighted in several recent reviews [1–3]. At ultraviolet energies, numerous tantalates and niobates exhibit high quantum efficiencies (~15–50%) for the water-splitting reactions, such as reported for La-doped $NaTaO_3$ and $La_2Ti_2O_7$ [4–7]. The greatest fraction of solar energy falls at the visible-light energies, and thus a smaller and more optimally-sized bandgap is necessary for the efficient use of sunlight. Many current approaches exist, including non-oxide systems such as $AgInS_2$–$CuInS_2$–ZnS [8–11], or composite materials such as $SrTiO_3$:Rh-$BiVO_4$ [12]. However, metal oxides typically represent the material of choice owing to their greater inherent stability against photocorrosion, and also, to their known high quantum efficiencies [13]. Though, for early transition-metal oxides the valence band energies are typically much lower than needed compared to the O_2/H_2O redox couple, and thus only bandgap sizes greater than ~3 eV exhibit suitable conduction band energies compared to the H_2/H_2O redox couple [14].

A successful and growing approach to raise the valence band energies and decrease the bandgap sizes of metal oxides is to incorporate additional elements having d^{10} electron configurations. Thus, these mixed-metal oxides contain an early transition metal (e.g. Ta^{5+} and Nb^{5+}) in combination with a late transition metal (e.g. Ag^+) or early main group element (e.g. Pb^{2+}), such as found in $AgNbO_3$ [15] or $PbBi_2Nb_2O_9$ [16]. In these systems, the bandgap excitations are found to arise from a metal-to-metal charge transfer (MMCT) transition between electron-donating d^{10} and electron-accepting d^0 electron configurations. This lowers their bandgap sizes by ~0.5–1.5 eV compared to that of alkali-metal analogues, e.g., $AgNbO_3$ versus $NaNbO_3$, via the insertion of a new higher-energy valence band consisting of the filled d^{10} orbitals. Our efforts in this field have recently focused on $Cu^+(d^{10})$-containing solids [17], and which remain almost entirely unexplored for their optical properties and potential as visible-light photocatalysts. The valence bands formed by Cu $3d^{10}$ orbitals may potentially meet the thermodynamic requirements for water oxidation, but of course, other properties such as mobility of excited carriers or the presence of active surface sites may also ultimately be critical [14].

Presented herein is a re-investigation of the Cu_2O–Ta_2O_5 system, which was previously explored by Jahnberg in the late 80's [18–21] in the course of preparing new tantalum and niobium oxides containing α-U_3O_8-type layers of TaO_7 pentagonal bipyramids. These prior studies focused on the structural aspects

* Corresponding author. Fax: +1 919 515 5079.
E-mail address: Paul_Maggard@ncsu.edu (P.A. Maggard).

0022-4596/$ - see front matter © 2010 Elsevier Inc. All rights reserved.
doi:10.1016/j.jssc.2010.01.030

and synthetic challenges of preparing Cu(I)-tantalates in high purity owing to the possible existence of different stacking variants close in composition. Our research efforts were motivated to probe the high-purity syntheses of copper(I) tantalates, the relationship between their atomic and electronic structures, and as well, for their optical and photocatalytic properties. Within this system, we report the high-purity solid-state and flux synthesis of two copper(I) tantalates, $Cu_5Ta_{11}O_{30}$ (**1**) and $Cu_3Ta_7O_{19}$ (**2**), and their structural characterization by single-crystal and powder X-ray diffraction, respectively. In addition, their optical properties were investigated by UV–vis diffuse reflectance and transmittance techniques, and which were analyzed with respect to their calculated electronic structures.

2. Experimental section

2.1. Syntheses

Both solid-state and flux synthetic approaches were investigated in order to prepare $Cu_5Ta_{11}O_{30}$ and $Cu_3Ta_7O_{19}$ in high purity. Solid-state reactions were performed starting from Cu_2O (Alfa Aesar, >99.9%) and Ta_2O_5 (Alfa Aesar, >99.99%) loaded over a range of Cu_2O:Ta_2O_5 molar ratios from 1:1.5 to 1:3.5 (total weight=1 g). The reactants were ground together and heated in evacuated fused-silica tubes at 1000 °C for 5 days, consistent with previously reported procedures [20]. The products were characterized by powder X-ray diffraction (PXRD) in transmission mode on an Inel XRG 3000 diffractometer fitted with a CPS 120 position sensitive detector and using Cu $K\alpha_1$ radiation from a sealed tube X-ray source. Large crystals of $Cu_5Ta_{11}O_{30}$ suitable for single-crystal XRD were obtained using a 10% excess of Cu_2O, giving a ~5:10 molar ratio, and slow cooling (5 °C/h) from 1000 to 700 °C. The reaction was then allowed to radiatively cool to room temperature in the furnace. The excess Cu_2O, which showed up as red deposits on the wall of reaction container and in the product, was removed by washing with 1.5 M HCl.

In contrast, the yellow–green coloured product of the reactions loaded at 3:7 (Cu:Ta) molar ratio could not be fitted to the $Cu_3Ta_7O_{19}$ model that has been proposed based on a high-resolution electron microscopy (HREM) study [21]. The powder XRD data could instead be fitted to that for $Cu_5Ta_{11}O_{30}$ with the emergence of an additional strong reflection at around 2θ=~28.2° and a broadening and splitting of peaks at around 2θ=~28.7° (Figure S1, Supporting Information). A series of reactions loaded at from 7.3:11 to 5.5:11 (Cu:Ta) molar ratios showed (after washing) only $Cu_5Ta_{11}O_{30}$, while Cu-poorer reactions loaded closer to 3:7 (Cu:Ta) molar ratio (i.e., 3.2:7, 2.8:7, 2.5:7, 2.3:7, 2.1:7, and 2:7) always gave $Cu_5Ta_{11}O_{30}$ together with the additional peaks described above. Further, a decrease in the reaction temperatures to 800–900 °C, as well as different heating times (5–7 days), did not significantly alter the resulting products. The first synthesis of high-purity $Cu_3Ta_7O_{19}$ (according to powder XRD) was achieved using additional CuCl (Alfa Aesar, >99%) as a flux. The reactants were mixed at the 3:7 (Cu:Ta) molar ratio, combined with the CuCl flux at a 1:10 molar ratio, and heated to 800 °C for 5 days. The flux was washed from the product using 3 M NH_4OH, followed by washing with 1.5 M HCl, to give a homogeneous yellow powder. The powder XRD data of this product was similar to that calculated from the HREM model [21], and the structure was refined using the full-profile Rietveld method (see next section).

2.2. X-ray structural characterization

The structures of $Cu_5Ta_{11}O_{30}$ and $Cu_3Ta_7O_{19}$ phases were refined using single-crystal and powder XRD methods, respectively. High-resolution powder XRD data for $Cu_3Ta_7O_{19}$ were recorded at room temperature on a RIGAKU D/Max 2200 powder X-ray diffractometer using Cu $K\alpha_1$ radiation with a diffracted beam graphite monochromator. Data were collected in a 2θ range of 6–93° in 0.01° steps, with a dwell time of 4 s at each step. The structural refinement was performed using the full-profile Rietveld method within the FullProf program package [22]. The starting atomic positions were taken from the HREM model proposed by Jahnberg [21]. Initially, only the zero-point shift and scale factor were refined. The lattice constants were allowed to refine next, and was followed by refinement of the background parameters with a polynomial used in the fit that was increased

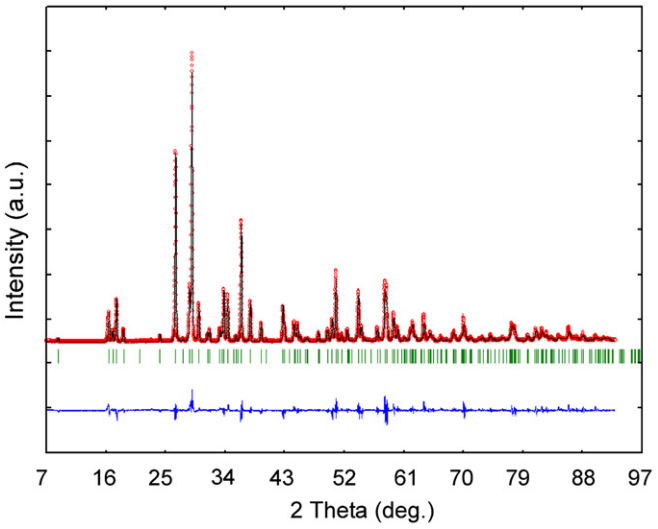

Fig. 1. PXRD and Rietveld refinement results for $Cu_3Ta_7O_{19}$. The observed profile is indicated by circles and the calculated profile by the solid line. Bragg peak positions are indicated by vertical tics. The difference diffractogram is shown at the bottom.

Table 1
Single crystal and powder X-ray refinement data for $Cu_5Ta_{11}O_{30}$ and $Cu_3Ta_7O_{19}$.

Compounds	$Cu_5Ta_{11}O_{30}$	$Cu_3Ta_7O_{19}$
fw	2781.48	1761.26
Space group, Z	$P\bar{6}2c$ (no. 190), 2	$P6_3/m$ (No.176), 2
Unit cell (Å), a	6.2252(1)	6.2278(1)
c	32.516(1)	20.1467(3)
V (Å^3)	1091.26(4)	672.7(1)
d_{calcd} (Mg/m^3)	8.465	8.643
Radiation	Mo $K\alpha$, λ=0.71073 Å	Cu $K\alpha$=1.54056 Å
μ (mm^{-1})	59.7	43.5
2θ range	5.02–77.02°	6.0–93.0°
No. of data collected	33070	8695 data points
No. of unique data	2015 (1618 with $F^2>2\sigma(F^2)$)	244 Bragg reflections
No. of variables	76	35
residuals[a]	$R_1(F^2>2\sigma(F^2))$=0.027 wR_2=0.049 R_1 (all data)=0.040, wR_2=0.052	R_B=0.058, R_{wp}=0.104, R_{exp}=0.049 χ^2=4.2

[a] $R_1=[\sum||F_0|-|F_c||/\sum|F_0|$, $wR_2=[\sum[w(F_0-F_0^2)^2]/\sum wF_0^4]^{1/2}$, $w^{-1}=[\sigma(F_0^2)+(Ap)^2+Bp]$, where $p=[\max(F_0^2,0)+2F_c^2]/3$, $R_B=\sum|I_0-I_c|/\sum I_0$, $R_{wp}=[\sum[w(y_0-y_c)]/\sum wy_0^2]^{1/2}$, $\chi_v^2=(R_{wp}/R_{exp})^2$.

up to the sixth order. Next, the atom positions were also allowed to refine, starting with the copper and tantalum atoms and then all oxygen atoms. This was followed by the addition of isotropic thermal parameters for all atoms. Afterwards, the profile-shape parameters were included with a peak asymmetry correction for $2\theta < 40^\circ$. The final refinement included 35 independent parameters (8695 data points) and converged at an R_B/R_{wp} =0.058/0.104. Shown in Fig. 1 is the resulting fit of the Rietveld refinement to the experimental powder XRD of $Cu_3Ta_7O_{19}$. Structure refinement parameters, atomic coordinates, and isotropic displacement parameters are given in Tables 1 and 2.

A Bruker-Nonius X8 Apex2 diffractometer was used for collecting single-crystal XRD data on $Cu_5Ta_{11}O_{30}$. A small ($0.08 \times 0.06 \times 0.04$ mm) irregular crystal was selected and mounted on a nylon loop using a small amount of Paratone N oil and cooled to 173 K. The unit cell dimensions were determined from a symmetry-constrained fit of 33,070 reflections in the range $5.02^\circ < 2\theta < 77.02^\circ$. The data collection strategy included both ω and φ scans that extended out to 2θ=80.32°. The reflection intensities were integrated with the SAINT subprogram in the SMART software package [23]. An empirical absorption correction was applied using the SADABS program [24]. A space group determination was made (*P*-62*c*, No. 190) and the structure was solved and refined using the SHELXTL 6.1 software package and associated subprograms [25]. The structure was refined by full-matrix least-squares on F^2 with anisotropic thermal parameters and converged to R_1/wR_2=0.040/0.052 and a goodness-of-fit=1.09. The structural refinement details and atomic positions are summarized in Tables 1 and 2, respectively.

2.3. Optical property measurements

The UV–vis diffuse reflectance spectra of $Cu_5Ta_{11}O_{30}$ and $Cu_3Ta_7O_{19}$ were collected on a Shimadzu UV–vis–NIR Spectro-

Table 2
Atomic coordinates, equivalent isotropic displacement parameters (Å^2), and site occupancies for $Cu_5Ta_{11}O_{30}$ and $Cu_3Ta_7O_{19}$.

Atom	Wyckoff position	Symmetry	*x*	*y*	*z*	*U*(eq)	Occ. ≠ 1
$Cu_5Ta_{11}O_{30}$							
Ta1	6*g*	.2	0.3627(1)	0	0	0.0050(1)	
Ta2	12*i*	1	0.6689(1)	0.9715(1)	0.1920(1)	0.0071(1)	
Ta3	4*f*	3	1/3	2/3	0.0972(2)	0.0117(1)	
Cu	12*i*	1	0.3337(3)	0.1637(2)	0.0952(1)	0.0120(2)	0.833[a]
O1	6*g*	.2	0.752(1)	0	0	0.010(1)	
O2	4*f*	3	1/3	2/3	0.9893(3)	0.005(1)	
O3	12*i*	1	0.370(1)	0.9419(9)	0.0596(1)	0.008(1)	
O4	12*i*	1	0.417(1)	0.084(1)	0.1901(2)	0.012(1)	
O5	4*f*	3	1/3	2/3	0.1961(2)	0.009(2)	
O6	4*e*	3	0	0	0.1808(2)	0.006(1)	
O7	6*h*	*m*	0.698(1)	0.961(1)	1/4	0.007(1)	
O8	12*i*	1	0.6108(8)	0.9115(9)	0.1300(1)	0.007(1)	
$Cu_3Ta_7O_{19}$							
Ta1	2*b*	–3	0	0	0	0.41(1)	
Ta2	12*i*	1	0.6945(2)	0.0292(2)	0.1564(1)	0.38(1)	
Cu	6*g*	–1	1/2	0	0	0.45(1)	
O1	12*i*	1	0.752(2)	0.036(3)	0.055(3)	0.21(1)	
O2	4*f*	3	2/3	1/3	0.128(1)	0.52(1)	
O3	12*i*	1	0.333(3)	0.902(2)	0.1544(5)	0.41(1)	
O4	4*e*	3	0	0	0.169(1)	0.64(1)	
O5	6*h*	*m*	0.715(2)	0.063(2)	1/4	0.19(1)	

[a] During the refinement the occupancy factor was fixed at the previously reported value of 0.833 (=5/6 for Cu^{1+}); and the site occupancy could be refined to a lower 0.815(4) without a statistically significant change in the final residuals.

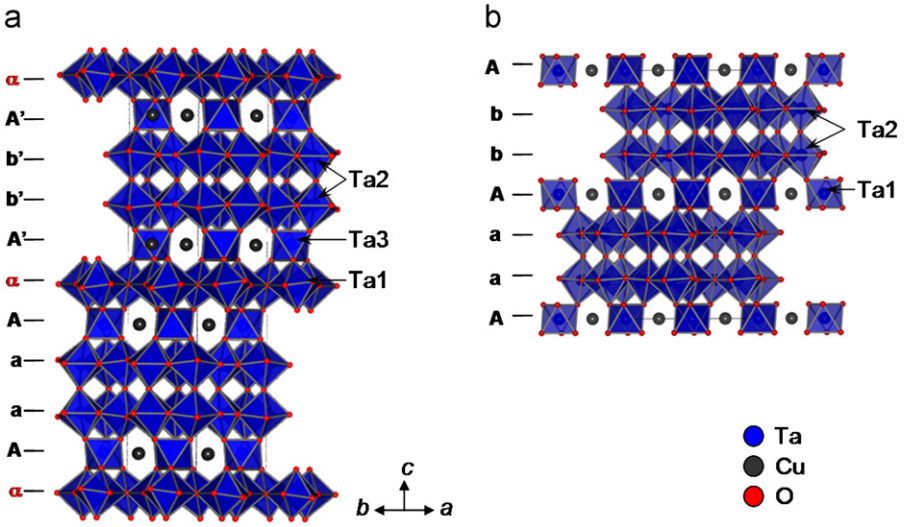

Fig. 2. Polyhedral views down [1 1 0] for $Cu_5Ta_{11}O_{30}$ and (b) $Cu_3Ta_7O_{19}$; blue polyhedra are TaO_7 pentagonal bipyramids and TaO_6 octahedra.

photometer (UV-3600) equipped with an integrating sphere. Approximately 50 mg of each sample was mounted onto a holder by pressing the powder into a $BaSO_4$ matrix and placing it along the external window of the integrating sphere. Pressed barium–sulfate powder was used as the reference and the data were plotted as the remission function $F(R_\infty)=(1-R_\infty)^2/(2R_\infty)$, where R is diffuse reflectance based on the Kubelka–Monk theory of diffuse reflectance [26]. Transmittance spectra for pressed pellets of each powdered sample were measured in the wavelength range of 200 – 800 nm at room temperature. Each solid-state compound was measured twice with two different pellet thicknesses, as detailed previously [27], in order to account for the regular reflection losses at the boundary surfaces in the transmittance measurements. Resultant absorption spectra were calculated using the Lambert law and evaluated as α (cm^{-1}) vs. wavelength (nm): $\alpha=(1/\Delta x)(\log(1/R_2)-\log(1/R_1))$; where α is the absorption coefficient in cm^{-1}; and $\Delta x=x_2-x_1$, where x_1 and x_2 are the thicknesses of the two sample pellets.

2.4. Thermal analysis

The thermal stability and decomposition of $Cu_3Ta_7O_{19}$ were measured on a TA Instruments SDT 2960 Simultaneous DSC-TGA under flowing nitrogen gas by heating to ~1100 °C at a programmed rate of 10 °C/min. A weighed amount (35–45 mg) was loaded onto a pan, equilibrated and tared at room temperature, and the data plotted as temperature (°C) versus heat flow (mW). Solid-state products obtained after heating to ~1000 °C were characterized by powder XRD in transmission mode, as described above.

2.5. Electronic structure calculations

The electronic structures were calculated using the linear muffin-tin orbital (LMTO) method in the atomic sphere approximation (ASA) with the tight-binding program TB–LMTO–ASA [28]. The radii of the Wigner–Seitz (WS) spheres were assigned automatically so that the overlapping potentials would be the best possible approximations to full potentials. Because both structures are rather open, special care was taken in filling the interatomic space. Using only atom-centered spheres resulted in errors because of the default 16% overlap restriction [29]. Therefore, empty-interstitial spheres (ES) were added to the crystal potential and the basis set. The sphere radii and their positions were chosen so that space filling was achieved without exceeding a sphere overlap of 16%. All sphere positions and radii were calculated automatically; the WS radii [Å] were Cu, 1.31 and 1.29; Ta, 1.29–1.35 and 1.30–1.35; O, 0.90–1.04 and 0.90–1.06; ES, 0.74–1.32 and 0.63–1.25 for $Cu_5Ta_{11}O_{30}$ and $Cu_3Ta_7O_{19}$. The calculations used a basis set of Cu—4*s*/4*p*/3*d*, Ta—6*s*/6*p*/5*d* and O—2*s*/2*p*-orbitals and the reciprocal space integrations were performed on $12\times12\times12$ grids of irreducible *k*-points using the tetrahedron method [30]. Semi-empirical extended Hückel calculations were performed by the program package CAESAR [31] with the following parameters (double zeta-functions): H_{ij} (eV), ζ_1, coefficient 1, ζ_2, coefficient 2: Cu: 4*s*—11.40, 2.20, 1.00, 0, and 0; 4*p*—6.06, 2.20, 1.00, 0, and 0; 3*d*—14.00, 5.95, 0.5933, 2.300, and 0.5744; Ta: 6*s*—10.10, 2.28, 1.00, 0, and 0; 6p—6.86, 2.241, 1.00, 0, and 0; 5*d*—12.10, 4.762, 0.6815, 1.938, and 0.5589;

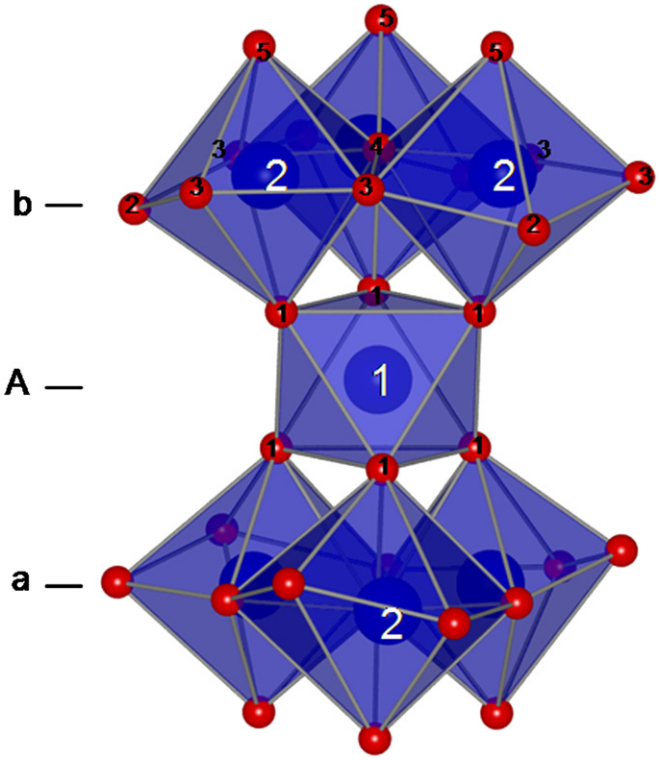

Fig. 4. The local coordination environment in $Cu_3Ta_7O_{19}$ for a TaO_6 octahedron, formed from three edge-sharing pentagonal bipyramids both above and below. Atom types are numbered for O (red) and Ta (blue polyhedra). For interpretation of the references to colour in this figure legend, the reader is referred to the web version of this article.

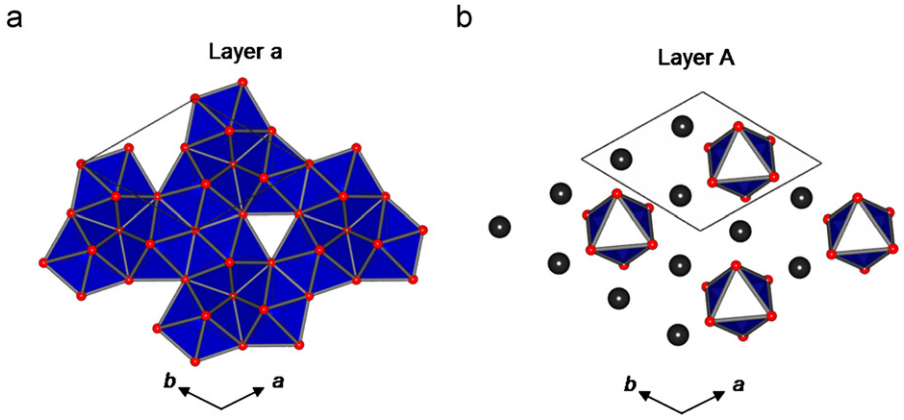

Fig. 3. Structural views down [0 0 1] of $Cu_3Ta_7O_{19}$ and $Cu_5Ta_{11}O_{30}$ for (a) a single layer of TaO_7 pentagonal bipyramids and, (b) an intervening layer of TaO_6 octahedra and Cu atoms.

O: 2*s*—32.29999, 2.2775, 1.00, 0, and 0; 2*p*—14.80, 2.275, 1.00, 0, and 0.

3. Results and discussion

3.1. Syntheses

The Cu_2O–Ta_2O_5 phase diagram was initially explored by Jahnberg [18–21] in the temperature range of 800–1100 °C, and the products were characterized using powder X-ray diffraction (PXRD) and high-resolution electron microscopy (HREM). In these studies, the most predominant product over the entire compositional range found was $Cu_5Ta_{11}O_{30}$. The existence of only one other well-ordered phase, $Cu_3Ta_7O_{19}$, was found in the HREM investigations [21]. However, this phase could only be obtained as a side-product. Similarly, solid-state reactions performed herein using Cu:Ta molar ratios from 7.3:11 to 5.5:11 were found to contain only the $Cu_5Ta_{11}O_{30}$ phase. Large crystals could be grown using 10% excess Cu_2O and were suitable for single-crystal XRD. However, Cu-poorer reactions loaded closer to 3:7 (Cu:Ta) molar ratio (3.2:7, 2.8:7, 2.5:7, 2.3:7, 2.1:7, and 2:7) always gave $Cu_5Ta_{11}O_{30}$ together with some unidentified peaks. However, the use of a molten CuCl flux resulted here in the first high-purity synthesis of $Cu_3Ta_7O_{19}$, which enabled its structural characterization by PXRD. The differential scanning calorimetry results (Fig. 2S2, Supporting Information) show that $Cu_3Ta_7O_{19}$ is stable up to ~900 °C, whereupon it decomposes irreversibly to a mixture of Cu_2O, Ta_2O_5 and $Cu_5Ta_{11}O_{30}$.

3.2. Structural descriptions

The basic structural features of $Cu_5Ta_{11}O_{30}$ (**1**) and $Cu_3Ta_7O_{19}$ (**2**) have been described previously [18–21]. Results of our single-crystal and powder XRD refinements, Tables 1 and 2, closely match with the previously proposed crystal structures. The polyhedral structural views of **1** and **2** down ~[1 1 0] are shown in Fig. 2. Both structures contain layers of edge-shared TaO_7 pentagonal bipyramids, Fig. 3a, that are structurally similar to those first found in α-U_3O_8 [32]. These layers stack along *c*-axis, sharing apex O1 atoms and forming both single (labeled α) and double layers (labeled a/b') in **1**, and only double layers (labeled a/b) in **2**. These alternate with layers of TaO_6 octahedra and linearly-coordinated Cu^+ (labeled A/A′), and shown separately in Fig. 3b. The TaO_6 octahedra are formed from the apical O atoms from three edge-shared pentagonal bipyramids both above and below, Fig. 4. The three apical oxygen atoms are tilted towards each other in order to form a more regular octahedral coordination environment, causing a distortion of the edge-shared O atoms in the plane of the TaO_7 pentagonal bipyramids. There are three Cu atoms per TaO_6 octahedron in the A/A′ layer, and which bond to two apical O atoms in adjacent layers above and below to form the linear coordination geometry.

Although both **1** and **2** share generally similar structural features, a single layer of pentagonal bipyramids (α) in **1** interleaves the repeating {AaaAbbA} layer pattern found in **2**, Fig. 2. This causes a displacement of the A layer (TaO_6/Cu+) along $\vec{a}' = \vec{a} + \vec{b}$ by 1/2 translation and yields the longer repeating sequence {AaaAαA′b′b′A′} in **1**. Further, the new Wyckoff site

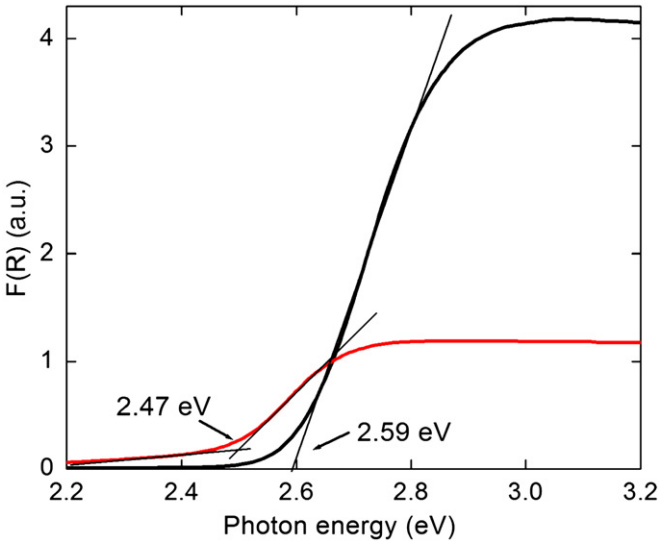

Fig. 5. Measured UV–vis diffuse reflectance spectra for $Cu_5Ta_{11}O_{30}$ (black) and $Cu_3Ta_7O_{19}$ (red), with the onset of the absorption edges labeled. For interpretation of the references to colour in this figure legend, the reader is referred to the web version of this article.

Table 3
Selected interatomic distances in $Cu_5Ta_{11}O_{30}$ and $Cu_3Ta_7O_{19}$.

$Cu_5Ta_{11}O_{30}$			$Cu_3Ta_7O_{19}$		
A–B	Distance (Å)		A–B	Distance (Å)	
Ta1, pentagonal bipyramid			Ta1, octahedron	×6	
Ta1–O1	1.999(6)	×2	Ta1–O1	2.003(5)	
Ta1–O1	2.422(8)	×1	Ta2, pentagonal bipyramid		
Ta1–O2	2.020(2)	×2	Ta2–O1	2.071(3)	×1
Ta1–O3	1.975(4)	×2	Ta2–O2	2.068(4)	×1
Ta2, pentagonal bipyramid			Ta2–O3	1.979(6)	×1
Ta2–O4	1.994(7)	×1	Ta2–O4	2.016(2)	×1
Ta2–O4	2.413(5)	×1	Ta2–O5	1.895(3)	×1
Ta2–O4	2.013(7)	×1	Ta2–O3	1.984(1)	×1
Ta2–O5	2.005(6)	×1	Ta2–O3	2.508(5)	×1
Ta2–O6	2.012(1)	×1	Cu coordination		
Ta2–O7	1.898(1)	×1	Cu–O5	1.841(4)	×2
Ta2–O8	2.048(4)	×1			
Ta3, octahedron					
Ta3–O3	2.022(6)	×3			
Ta3–O8	1.953(4)	×3			
Cu coordination					
Cu–O3	1.900(5)	×1			
Cu–O8	1.894(4)	×1			

multiplicity (12*i*) for Cu^+ in the A layer of **1** means that the position can only be fractionally occupied (~5/6) to give the charge-balanced $Cu_5Ta_{11}O_{30}$ stoichiometry, as confirmed by single-crystal XRD herein. An unfixed refinement of the Cu-site occupancy gives a very close 0.815(4) occupancy. However, the possibility remains that Cu could fully occupy the 12*i* site at other loaded stoichiometries, and would result in a partial reduction of the structure. Our preliminary results in this direction seem to suggest that this is unlikely, as reactions loaded more Cu_2O-rich yielded only the large single crystals of $Cu_5Ta_{11}O_{30}$ that were characterized by single-crystal XRD. Listed in Table 3, the Cu–O distances of 1.895 and 1.841 Å in **1** and **2**, respectively, are comparable to those in earlier reported Cu(I) oxides. For example, the Cu–O distance is 1.849 and 1.835 Å in Cu_2O and $CuFeO_2$ [33,34], respectively. The Cu–Cu distances are at a much longer ~3.115 Å in **1** and ~3.114 Å in **2**.

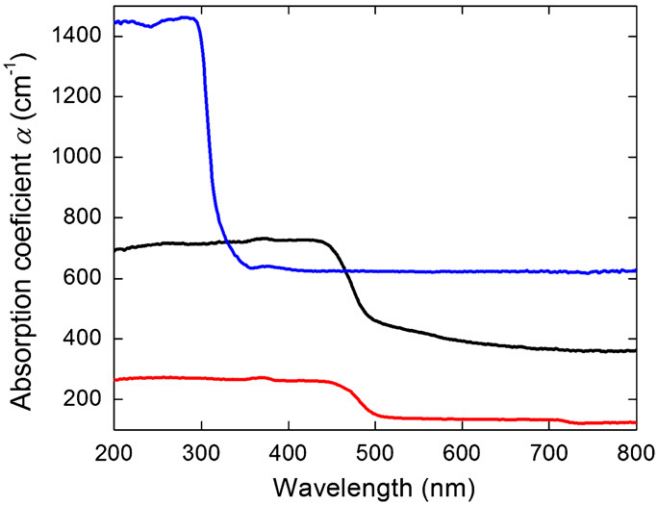

Fig. 6. Calculated absorption coefficient spectra for $Cu_5Ta_{11}O_{30}$ (black), $Cu_3Ta_7O_{19}$ (red) and $NaTaO_3$ (blue). For interpretation of the references to colour in this figure legend, the reader is referred to the web version of this article.

Several similar alkali and alkaline-earth analogues of these structures exist containing single and double layers of pentagonal bipyramids. Both $Na_2Nb_4O_{11}$ and $CaTa_4O_{11}$ contain only single layers of TaO_7 pentagonal bipyramids that alternate with layers of TaO_6 octahedra formed by the apical O atoms [35]. As in **1** and **2**, the layers of edge-shared TaO_7 pentagonal bipyramids are slightly undulated with O atoms shifted slightly out of the equatorial plane. This tilting in $Na_2Nb_4O_{11}$ and $CaTa_4O_{11}$ displaces the O atoms closer to Na and Ca, causing Na to be 7-coordinate and Ca to be 8-coordinate. By contrast, the Cu^+ coordination geometry in **1** and **2** remain unaltered by this tilt. In $CeTa_7O_{19}$ [36], only double layers of pentagonal bipyramids are found, which are separated by TaO_6 octahedra and 8-coordinate Ce. The Ta–O and

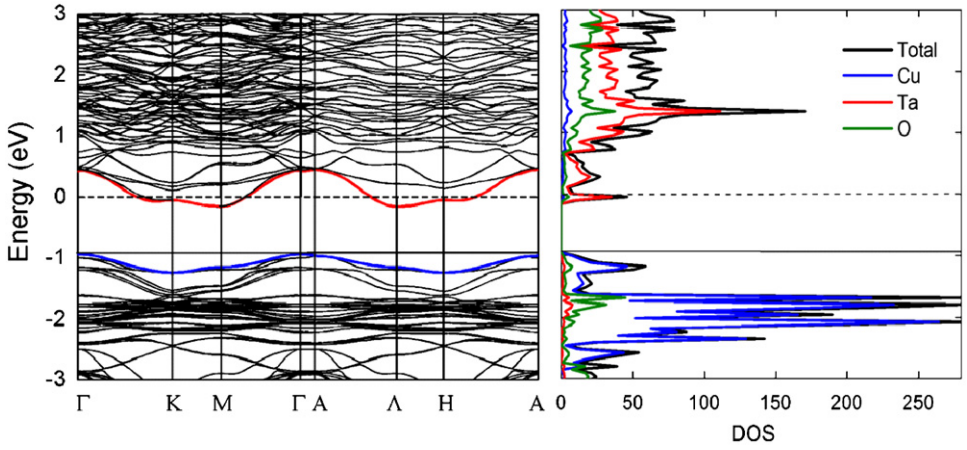

Fig. 7. Results of TB–LMTO–ASA electronic structure calculations for $Cu_5Ta_{11}O_{30}$, including the band structure diagram (left) and total and partial densities-of-states for each element (right). The Fermi level is labeled by the solid horizontal line, while the Fermi level for the hypothetical '$Cu_6Ta_{11}O_{30}$' is labeled by the dashed horizontal line.

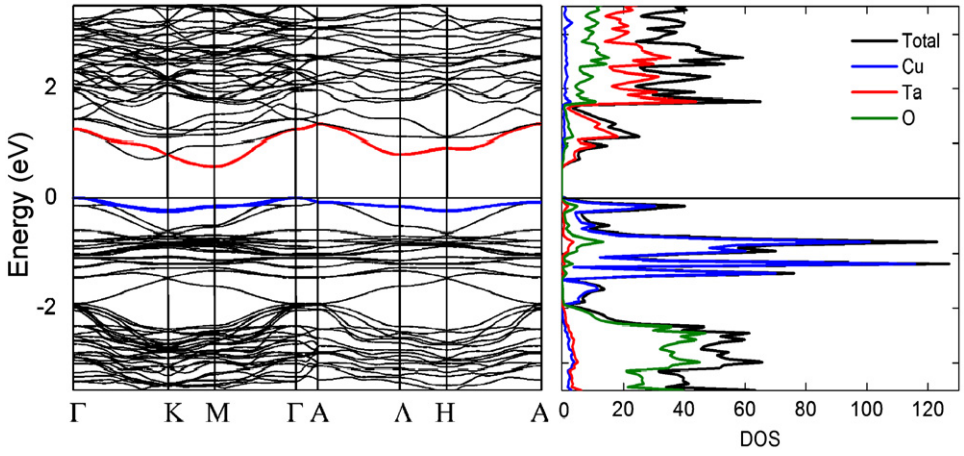

Fig. 8. Results of TB–LMTO–ASA electronic structure calculations for $Cu_3Ta_7O_{19}$, including the band structure diagram (left) and total and partial densities-of-states for each element (right).

O–O distances in these examples are all in close agreement with those in **1** and **2**, listed in Table 3.

3.3. Optical properties

Transition-metal oxides combining a d^{10} (e.g., Cu^{+}, Ag^{+}) and a d^{0} (e.g., Nb^{5+}, Ta^{5+}) electron configuration have drawn increasing attention owing to their potentially low-energy visible-light absorptions that arise from a metal-to-metal charge transfer (MMCT) transition [1,2,15–17]. Thus, UV–vis diffuse reflectance spectra (DRS) for $Cu_5Ta_{11}O_{30}$ (**1**) and $Cu_3Ta_7O_{19}$ (**2**) were measured to probe the effect of Cu^{+} on the bandgap sizes of tantalates, shown in Fig. 5. The bandgap sizes are ~2.59 eV for **1** and ~2.47 eV for **2**, consistent with the yellowish-orange colour of both powders. Bandgap sizes for alkali–metal tantalates are in the range of ~3.5 to >4.0 eV, while for silver tantalate (e.g. $AgTaO_3$) the bandgap size is ~3.4 eV [15]. The incorporation of higher-energy $3d^{10}$ (Cu+) orbitals in **1** and **2** has further lowered their bandgap sizes deeply into the visible-light energies. Small differences in the diffuse reflectance of sub-bandgap light likely owes to the crystallite sizes, where smaller particle sizes are known to increase the diffuse reflectance [27a].

The optical absorption coefficient, α (cm^{-1}), of a solid determines the rate of light absorption as a function of depth, where at α^{-1} the light intensity drops to ~36% of its starting intensity; for example, a low α leads to light being poorly absorbed in a material. Generally, semiconductors exhibit a sharp edge in their absorption coefficient spectra, since photons with energy below the bandgap size do not have sufficient energy to excite an electron across the band gap. Thus, α depends both on the solid and on the wavelength of light. Measured values of α for **1** and **2** are plotted in Fig. 6 as a function of wavelength and are compared to that of $NaTaO_3$. The La-doped $NaTaO_3$ is one of the most efficient known UV-active photocatalysts [4–6], and is shown here to absorb light at the band edge much more strongly ($\alpha \sim 1450\,cm^{-1}$) than either **1** or **2** ($\alpha \sim 700\,cm^{-1}$ for **1** and $\sim 275\,cm^{-1}$ for **2**). Structurally, $NaTaO_3$ contains vertex-shared TaO_6 octahedra in a distorted perovskite type, in contrast to the layers of TaO_7 pentagonal bipyramids in **1** and **2**. Further, the structure of **1** contains a larger fraction of TaO_6 octahedra as compared to the structure of **2**, owing to the single layers of pentagonal bipyramids. Although the bandgap sizes fall more deeply into the visible-light energies, their absorption coefficients are 2–5 × smaller.

3.4. Electronic structure calculations

Understanding the electronic origin of the bandgap sizes in $Cu_5Ta_{11}O_{30}$ (**1**) and $Cu_3Ta_7O_{19}$ (**2**) is essential to determine whether their electronic structures are thermodynamically favorable for the photodecomposition of water. In order to be compatible for the visible-light photocatalysis of water, the valence-band energy level of La-doped $NaTaO_3$, for example, must be raised by ~1.0–2.0 eV closer to the conduction-band energy level (and to the O_2/H_2O redox couple), as described before [1,4]. This is a major limitation for achieving visible-light photocalalysis in many other early transition-metal oxides as well [1–3]. Thus, the electronic structures of **1** and **2** were calculated in order to determine the structural origin and effects of the layers of TaO_7 pentagonal bipyramids, as well as the addition of Cu^{+} atoms, on their valence and conduction band energies.

The total and projected densities of states (DOS) and corresponding band structures were calculated for both **1** and **2** using the the linear muffin-tin orbital (LMTO) approach, shown in Figs. 7 and 8, respectively. The Fermi levels are labeled with solid lines according to their compositions, while the Fermi level for the hypothetical '$Cu_6Ta_{11}O_{30}$' (i.e., with a full Cu-site occupancy) is

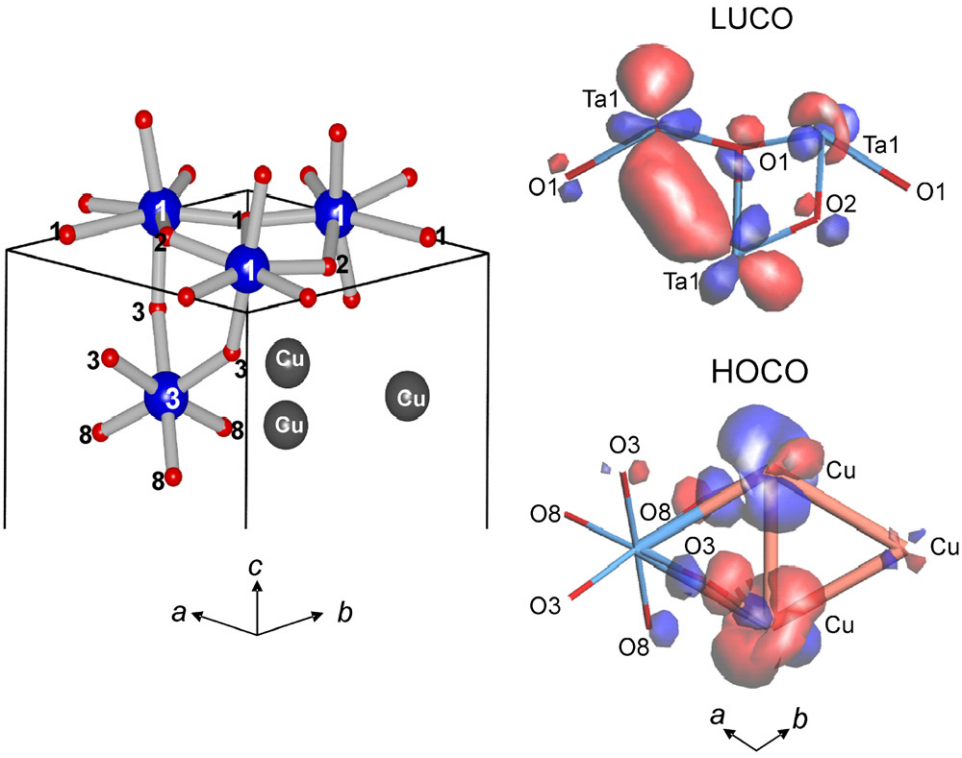

Fig. 9. On the right, the calculated highest-occupied crystal orbital (HOCO) and lowest-unoccupied crystal orbital (LUCO) for $Cu_5Ta_{11}O_{30}$; on the left, a wedge of the structure that contains the HOCO and LUCO atoms, with the atom types and the unit cell labeled for comparison. Blue circles are Ta, red are O and grey are Cu. For interpretation of the references to colour in this figure legend, the reader is referred to the web version of this article.

labeled as a dashed line in **1**. For **1**, the hypothetical full occupancy of the Cu site would lead to metallic behavior owing to a partial filling of Ta *d*-orbitals. In each case, the lowest-energy bandgap excitation is predicted to be indirect (i.e., $\Gamma \rightarrow M$ or Λ for **1**, and $\Gamma \rightarrow M$ for **2**), and which is consistent with the smaller absorption coefficients measured for **1** and **2** compared to that for $NaTaO_3$ (above). However, the bandgap sizes of metal oxides are generally calculated to be smaller than that obtained experimentally [37,38], and which were calculated here to be ~0.85 eV and ~0.55 eV for **1** and **2,** respectively. However, the predicted larger bandgap size for **1** is in agreement with experiment, being found for the structure with the incomplete Cu-site occupation. The insertion of higher-energy Cu 3*d*-orbitals into their electronic structures has helped to lower the bandgap sizes of each by ~1.5 eV compared to $NaTaO_3$. This represents an even more significant lowering of the bandgap size than known for $AgTaO_3$ (3.4 eV), owing to the higher-energy 3*d* (Cu^+) versus 4*d* (Ag^+) orbitals.

For both **1** and **2**, the highest energy valence bands comprised of Cu $3d^{10}$ orbitals (blue projection), while the lowest-unoccupied conduction bands consist of Ta $5d^0$ orbitals (red projection). Plots of the highest-occupied and lowest-unoccupied crystal orbitals within the structures of **1** and **2** are shown in Figs. 9 and 10, respectively, according to the tight-binding approach. The highest-occupied crystal orbital in each corresponds to filled $3d_{z^2}$ orbitals on Cu with some mixing with the O 2*p*-orbitals that are bridging to TaO_7 and TaO_6 polyhedra. The lowest-unoccupied crystal orbital in each derives from the in-plane Ta $5d_{xy}/5d_{x^2-y^2}$ orbitals of TaO_7 pentagonal bipyramids, rather than the TaO_6 octahedra, as well as some mixing with the O 2*p*-orbitals. Thus, the lowest-energy bandgap excitations of **1** and **2** proceed by metal-to-metal charge transfer (MMCT) transitions between the linearly-coordinated Cu and the layers of TaO_7 pentagonal bipyramids. This is in contrast to $NaTaO_3$, where the bandgap transition involves primarily the O 2*p*-orbitals and Ta 5*d*-orbitals located within TaO_6 octahedra. Under similar photocatalysis testing conditions as used for $NaTaO_3$ [4–6], **1** and **2** have so far proven inactive for either O_2 or H_2 production in water. Thus, while a much lower bandgap size has been achieved from a MMCT between Cu 3*d* and Ta 5*d*-orbitals, the effect of the layers of pentagonal bipyramids has been detrimental to photocatalytic activity. Possible reasons could include a low mobility of the excited carriers and/or a change in the surface active sites that impairs the reaction kinetics.

4. Conclusions

The copper(I) tantalates, $Cu_5Ta_{11}O_{30}$ (**1**) and $Cu_3Ta_7O_{19}$ (**2**), have been prepared in high purity using solid-state and flux

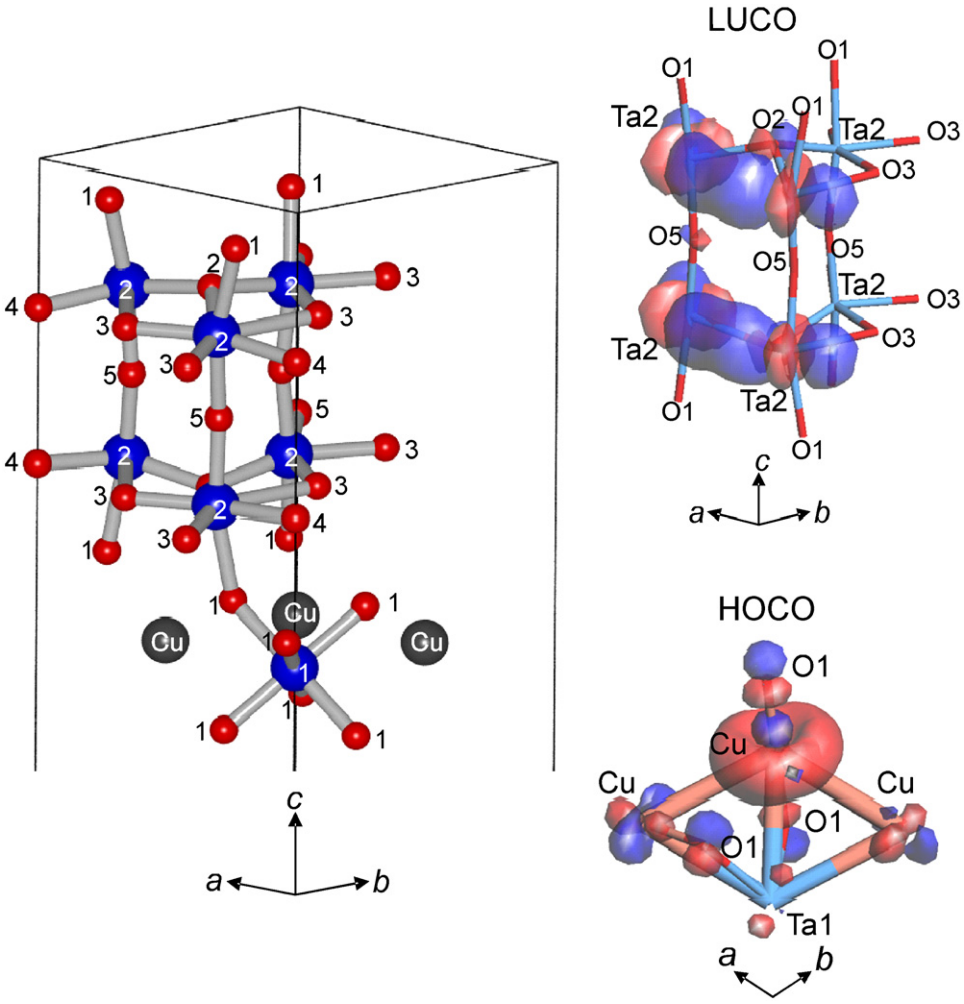

Fig. 10. On the right, the calculated highest-occupied crystal orbital (HOCO) and lowest-unoccupied crystal orbital (LUCO) for $Cu_3Ta_7O_{19}$; On the left, a wedge of the structure that contains the HOCO and LUCO atoms, with the atom types and the unit cell labeled for comparison. Blue circles are Ta, red are O and grey are Cu. For interpretation of the references to colour in this figure legend, the reader is referred to the web version of this article.

synthetic methods, respectively. Their structural characterizations by single-crystal and powder XRD are consistent with previous reports, and contain single and double layers of edge-shared TaO_7 pentagonal bipyramids that alternate with a layer of Cu^+ and TaO_6 octahedra. Compared to $NaTaO_3$, the addition of Cu 3*d*-orbitals results in significantly smaller bandgap sizes of ~2.59 eV for **1** and ~2.47 eV for **2**, but also 2–5 times smaller optical absorption coefficients. Their lowest-energy bandgap transitions are predicted to be indirect, and originate from a MMCT between primarily the Cu 3*d* and Ta 5*d*-orbitals within the TaO_7 pentagonal bipyramids (each mixed with some O 2*p*-orbital contributions). A growing number of known visible-light photocatalysts have been reported to be driven by similar MMCT transitions (e.g. $AgNbO_3$). Thus, this work shows the significant potential of Cu(I)-containing oxides in significantly lowering the bandgap sizes of early transition-metal oxides, even though these still remain relatively unexplored.

Supporting Information Available

Comparison of experimental and theoretical powder patterns at different Cu_2O:Ta_2O_5 molar ratios and DSC curves for $Cu_5Ta_{11}O_{30}$. The crystallographic information file can be obtained from the Fachinformationzentrum Karlsruhe, 76344 Eggenstein–Leopoldshafen, Germany (e-mail: crysdata@fiz.karlsruhe.de) on quoting the Registry nos. CSD-421398.

Acknowledgments

The authors acknowledge support of this research from the donors of the American Chemical Society Petroleum Research Fund (#46803-AC10), and from the Chemical Sciences, Geosciences and Biosciences Division, Office of Basic Energy Sciences, Office of Science, US Department of Energy (DE-FG02-07ER15914), and also assistance with the collection of single-crystal X-ray data (P. Boyle) and high-resolution powder XRD data (H.-C. zur Loye).

Appendix A. Supplementary materials

Supplementary data associated with this article can be found in the online version at doi:10.1016/j.jssc.2010.01.030.

References

[1] [a] A. Kudo, Pure Appl. Chem. 79 (2007) 1917;
[b] Y. Miseki, A. Kudo, Chem. Soc. Rev. 38 (2009) 253.
[2] F.E. Osterloh, Chem. Mater. 20 (2008) 35.
[3] K. Domen, J.N. Kondo, M. Hara, T. Takata, Bull. Chem. Soc. Jpn. 73 (2000) 1307.
[4] H. Kato, K. Asakura, A. Kudo, J. Am. Chem. Soc. 125 (2003) 30082.
[5] A. Iwase, H. Kato, A. Kudo, Chem. Lett. 34 (2005) 945.
[6] D.G. Porob, P.A. Maggard, J. Solid State Chem. 179 (2006) 1727.
[7] [a] H.G. Kim, D.W. Hwang, S.W. Bae, J.H. Jung, J.S. Lee, Catal. Lett. 91 (2003) 193;
[b] D. Arney, B. Porter, B. Greve, P.A. Maggard, J. Photochem. Photobiol. A 199 (2008) 230.
[8] A. Kudo, I. Tsuji, H. Kato, Chem. Commun. (2002) 1958.
[9] [a] I. Tsuji, H. Kato, H. Kobayashi, J. Am. Chem. Soc. 126 (2004) 13406;
[b] I. Tsuji, H. Kato, H. Kobayashi, J. Phys. Chem. B 109 (2005) 7323.
[10] I. Tsiji, H. Kato, A. Kudo, Angew. Chem., Int. Ed. 44 (2005) 3565.
[11] I. Tsiji, H. Kato, A. Kudo, Chem. Matter. 18 (2006) 1969.
[12] A. Kato, M. Hori, Y. Konta, Y. Shimodaira, A. Kudo, Chem. Lett. 33 (2004) 1348.
[13] M. Woodhouse, B.A. Parkinson, Chem. Soc. Rev. 38 (2009) 197.
[14] [a] D.E. Scaife, Solar Energy 24 (1980) 41;
[b] M. Grätzel (Ed.), Energy Resources through Photochemistry and Catalysis, Academic Press, New York, 1983.
[15] H. Kato, H. Kobayashi, A. Kudo, J. Phys. Chem. B 106 (2002) 12441.
[16] H.G. Kim, D.W. Hwang, J.S. Lee, J. Am. Chem. Soc. 126 (2004) 8912.
[17] H. Lin, P.A. Maggard, Inorg. Chem. 48 (2009) 8940.
[18] L. Jahnberg, Mater. Res. Bull. 16 (1981) 513.
[19] L. Jahnberg, J Solid State Chem. 41 (1982) 286.
[20] L. Jahnberg, Acta Chem. Scand. A 41 (1987) 527.
[21] L. Jahnberg, M. Sunberg, J. Solid State Chem. 100 (1992) 212.
[22] J. Rodriges–Carvajal Program: FullProf. Lab. Leon Brillouin, CEA-CNRS, 1998.
[23] SMART, Bruker AXS, Madison, WI, 1996.
[24] R.H. Blessing, Acta Crystallogr. A 51 (1995) 33.
[25] SHELXTL, Bruker AXS, Inc., Madison, WI, 2000.
[26] W.W. Wendlandt, H.G. Hecht, Reflectance Spectroscopy, Intersciences, New York, 1996.
[27] [a] G. Kortüm, Reflectance Spectroscopy, Springer-Verlag, New York, 1969;
[b] H. Lin, X. Wu, P.A. Maggard, Inorg. Chem., in press (ASAP).
[28] R, Tank, O. Jepsen, A. Burkhardt, O.K. Andersen, TB-LMTO-ASA Program, Vers. 4.7; Max-Plank-Institut für Festkörperforschung: Stuttgart, Germany, 1995.
[29] O. Jepsen, O.K. Andersen, Z. Phys. B 97 (1995) 35.
[30] [a] O.K. Andersen, O. Jepsen, Solid State Commun. 9 (1971) 1763;
[b] P. Bloechl, O. Jepsen, O.K. Andersen, Phys. Rev. B. 34 (1994) 16223.
[31] J. Ren, W. Liang, M.-H. Whangbo, CAESAR, PrimeColor Software Inc., Raleigh, NC, USA, 1998.
[32] B.O. Loopstra, Acta Crystallogr. 17 (1964) 651.
[33] H.E. Swanson, R.K. Fuyat, Nat. Bur. Stand. (US) Circ. 539 (1953) (Cu_2O).
[34] C.T. Prewitt, R.O. Shannon, D.B. Rogers, Inorg. Chem. 10 (1971) 119.
[35] L. Jahnberg, J. Solid State Chem. 1 (1970) 454.
[36] B.M. Gatehouse, J. Solid State Chem. 27 (1979) 209.
[37] J. Carrasco, F. Illas, N. Lopez, E.A. Kotomin, Y.F. Zhurovskii, R.A. Evarestov, Y.A. Masrikov, S. Piskunov, Mater. J. Phys. Rev. B 73 (2006) 064106.
[38] S. Piskunov, E. Heifets, R.I. Eglitis, B. Borstel, Comput. Mater. Sci. 29 (2004) 165.